Hydrothermal synthesis of Cu-substituted Ni ferrites: Structural, morphological, and magnetic properties

Roberto Nisticò [a,*], Roberto Mantovan [b], Matteo Cantoni [c], Christian Rinaldi [c], Mery Malandrino [d], Silvia Mostoni [a], Massimiliano D'Arienzo [a], Barbara Di Credico [a], Roberto Scotti [a,e]

[a] *Department of Materials Science, INSTM, University of Milano-Bicocca, Via R. Cozzi 55, 20125 Milano, Italy*
[b] *CNR-IMM, Unit of Agrate Brianza, Via. C. Olivetti 2, 20864 Agrate Brianza, MB, Italy*
[c] *Department of Physics, Politecnico di Milano, Via. G. Colombo 81, 20133 Milano, Italy*
[d] *Department of Chemistry, University of Torino, Via P. Giuria 7, 10125 Torino, Italy*
[e] *Institute for Photonics and Nanotechnologies-CNR, Via alla Cascata 56/C, 38123 Povo, TN, Italy*

ARTICLE INFO

ABSTRACT

Cu-substituted Ni ferrite systems are produced following a hydrothermal synthetic route carried out at relatively mild conditions (*i.e.*, below 200 °C). Different degrees of substitution were investigated, ranging from bare Ni ferrite to a complete Cu-substituted system (by replacing 100% of Ni with Cu). Morphological and structural characterisations point out that the introduction of Cu in the Ni ferrite (below 50% substitution) causes a gradual reduction of the average diameter of the ferrite polyhedral nanoparticles maintaining the Ni ferrite structure. At higher content of Cu, instead, the morphology evolves toward the co-presence of iron oxides (magnetite and hematite) and copper oxide (tenorite), without the formation of bare Cu ferrite. The partially substituted Ni ferrite nanomaterials exhibit a mostly superparamagnetic behaviour in all samples, registering a reduction of the values of magnetisation saturation by increasing the Cu content. Transmission Mössbauer spectroscopy performed on these nanomaterials evidenced a gradual lowering of the Fe fraction occupying the octahedral sites and a consequent increment of the Fe fraction in the tetrahedral sites. Quantitative analysis confirms the gradual reduction of the Ni content within the ferrite samples, coupled with the opposite increment of the Cu content, whereas the Fe content is lower in the case of Ni75-Cu25 sample. This particular behaviour can be associated with the influence of Cu substitution in the Ni ferrite structure, with preferential replacement of Fe from the octahedral B-sites toward the tetrahedral A-sites.

1. Introduction

In the last decades, the new frontier in materials science is the design of intelligent (smart) nanomaterials able to show properties variation/modulation/control by simply applying an external stimulus (*i.e.*, stimuli-responsive materials), such as variation of temperature, pressure, moisture, pH, chemical species, ionic strength, mechanical stress, light radiation, electric field, and magnetic field [1–12]. In this context, magnetic field (MF) responsive nanomaterials reached important results in several technological fields of emerging interest, such as biomedicine, magnetic resonance imaging, robotics, electronics, data and energy storage, environmental remediation processes, (photo)catalysis, spintronics, and many others [13–26]. The appearance of a strong magnetic

moment in MF-responsive nanomaterials is determined by both the electronic distribution (*i.e.*, electronic configuration) and motion (*i.e.*, electrons spin) [13] On this basis, there are only few chemical elements able to provide a strong magnetic response, namely: iron (Fe), cobalt (Co), nickel (Ni), manganese (Mn), chromium (Cr), and some rare earth metals [27–29]. In this context, ferrites are a class of ceramic oxides showing important magnetic features [30]. Additionally, ferrites are advantaged by having a small band gap (*approx.* 1.5–2.5 eV), which makes them promising substrates for a new generation of photo(electro) chemical devices [31–33].

Among the different classes of ferrites, both nickel ($NiFe_2O_4$) and copper ($CuFe_2O_4$) ferrites are MF-responsive nanomaterials of paramount interest as they actually find applications in many advanced

technological fields of research, ranging from photo(electro)catalysis for renewable fuels production [34–36], electronics [37], to environmental remediation processes [38]. In the case of nickel ferrite, this material has an inverse spinel structure, organized into 8-tetrahedral A-sites (containing Fe^{3+} cations), and 16-octahedral B-sites (containing both M^{2+} and Fe^{3+} cations, with M corresponding to the non-iron metal, namely Ni) per unit [39]. Vice versa, copper ferrite is organized as a partial inverse spinel structure with the degree of inversion depending on the heat treatment, but with a predominance of B-sites occupied by Cu^{2+} ions [40,41]. In the case of spinel ferrites, the complete chemical formula is the following: $[M^{2+}_{1-x}Fe^{3+}_x]^T[M^{2+}_xFe^{3+}_{2-x}]^OO^{2-}_4$, with apexes "T" and "O" referring respectively to tetrahedral A-sites and octahedral B-sites, and "x" representing the degree of inversion defined as the fraction of tetrahedral A-sites occupied by Fe^{3+} cations [39]. Due to the inverse spinel structure, the degree of inversion for pure nickel ferrite is equal to one. Furthermore, ions occupying the tetrahedral A-sites are defined as "network formers", whereas those occupying the octahedral B-sites are defined as "network modifiers". In the case of both nickel and copper ferrites, Ni^{2+} cations are considered as network modifiers, whereas Fe^{3+} and Cu^{2+} cations act as both network formers and modifiers [39,42].

Interestingly, both the nature and the amount of non-iron metal cations strongly influence most of the intrinsic properties of this class of ferrites [43]. In this context, the possibility of producing doped (quaternary) spinel ferrites containing more than one non-iron metal is rapidly emerging as a potential and powerful technological solution due to the prospect of merging the advantages of both bare systems, with the aim of creating novel MF-responsive nanomaterials with unique properties.

The scientific literature describing the correlation existing between the structural changes induced by the presence of dopant cations and the relative properties variation is quite broad. Concerning nickel ferrites, Ashiq *et al.* [44] reported the synthesis of Sb^{3+} substituted nickel ferrites obtained by reverse microemulsion techniques showing a metal-to-semiconductor transition temperature, and a room temperature (RT) resistivity variation as a function of the content in antimony cations. Since the electrical conduction of ferrites is due to the electrons hopping between iron cations occupying the octahedral B-sites [45], the partial replacement of iron with antimony at the octahedral B-sites caused primarily a reduction of the available number of ferric ions (with depletion of hopping electrons), and consequently an increment of the electrical resistivity. Rodrigues *et al.* [42], instead, investigated the synthesis of Co^{2+} substituted nickel ferrites by means of microwave-assisted combustion reactions. In their study, the resulting Co-Ni ferrites showed a reduction of the relative saturation magnetisation and a coupled increment of the coercivity values by increasing the content of cobalt ions. The reduction of the saturation magnetisation can be rationalised by considering the preference of Co^{2+} cations in replacing Ni^{2+} cations within the octahedral B-sites, whereas the increment in coercivity is a consequence of the increment of the domain wall energy. These two examples clearly demonstrate how the structural variation induced by introducing doping species in the ferrites lattice can dramatically affect the doped ferrite properties.

The interest on Cu-containing catalysts has rapidly increased over the recent years, as this metal is known being able to electrochemically catalyse specific reactions, such as the carbon dioxide conversion into C_2 valuable products (*i.e.,* carbon dioxide reduction reaction, CO_2RR) with acceptable efficiencies [46]. Furthermore, experimental evidences highlighted that Cu-containing catalysts (*e.g.,* copper ferrites) are also able to promote the carbon dioxide conversion toward C_2-C_3 products [47]. In this context, Khalaf *et al.* [48] investigated the possibility of integrating copper into nickel ferrites by following a synthetic route consisting into a combustion reaction in presence of citric acid as capping agent, obtaining Cu-Ni ferrites showing important features in the acetaldehyde electro-oxidation reaction.

Hence, this study aims at the introduction of Cu into the nickel ferrite structure following a low temperature wet synthesis approach, such as

the hydrothermal route carried out at mild conditions (*i.e.,* below 200 °C). In particular, different degrees of substitution were investigated (ranging from bare Ni ferrite to 100% Cu-substitution). Morphological, structural and magnetic features of samples were monitored by means of scanning electron microscopy coupled with energy dispersive X-ray spectroscopy probe (SEM-EDS), transmission electron microscopy (TEM), X-ray powder diffraction (XRD), vibrating sample magnetometry (VSM), transmission Mössbauer spectroscopy (TMS), and inductively coupled plasma optical emission spectroscopy (ICP-OES).

2. Experimental

2.1. Chemicals

Inorganic salts: Ferric nitrate nonahydrate ($Fe(NO_3)_3 \cdot 9 H_2O$, 98+% metal basis, crystalline contains excess HNO_3, CAS 7782–61-8, *Thermo-Scientific*), nickel nitrate hexahydrate ($Ni(NO_3)_2 \cdot 6 H_2O$, crystalline, CAS 13478–00-7, *Aldrich*), and copper nitrate trihydrate ($Cu(NO_3)_2 \cdot 3 H_2O$, puriss. p.a., 99–104%, CAS 10031–43-3, *Sigma-Aldrich*) are used as received. Potassium bromide (KBr, 99+%, FT-IR grade, CAS 7758–02-3, *Aldrich*) is heated at *approx.* 80 °C prior to use to maintain it dry.

Solutions and solvents: 6 M NaOH solution is prepared by dissolving sodium hydroxide pellets (NaOH, puriss., p.a., ACS reagent, ≥98%, CAS 1310–73-2, *Aldrich*) in deionized water. The resulting solution is stored in a fridge and maintained at *approx.* 5 °C. Acetone (CAS 67–64-1, *Sigma-Aldrich*) is used as received. Intermediate metal standard solutions were prepared from concentrated (1000 and 10,000 mg L^{-1}) stock solutions (*Sigma-Aldrich*, or *CPI International*) and acidified to pH = 1.5. Deionized water was used during the washing procedures. Milli-Q water with a resistivity of 18.2 MΩ cm was used. All chemicals were used without further purification.

2.2. Hydrothermal synthesis of nanomaterials

Nanomaterials are prepared following a modified procedure [49]. In a typical synthesis, the desired inorganic salts mixture (15 mmol) was dissolved in a fixed volume of distilled water (20 mL). Afterwards, 6 M NaOH solution (15 mL) is added to the mixture, reaching the final pH value of *ca.* 13, and registering the precipitation of the metal hydroxide in the alkaline medium. The final suspension was magnetically stirred for 30 min at RT. Subsequently, the mixture is transferred into a 125-mL sealed Teflon-lined autoclave Model 4748 (*Parr Instrument Company, Illinois, USA*), and thermally treated in a Carbolite CWF1200 muffle furnace (*Carbolite, Hope, UK*) with the following thermal program: (i) heating ramp from RT to 180 °C (heating rate: 10 °C min^{-1}), (ii) isothermal step at 180 °C for 12 h, and (iii) cooling step from 180 °C to 50 °C (cooling rate: 10 °C min^{-1}). Subsequently, the autoclave was allowed to cool down from 50 °C to RT naturally. The precipitate was magnetically separated from the solution by using a commercial neodymium magnet, and purified by washing several times with deionized water (four times) and acetone (one time) [50]. Finally, the resulting suspension was deposited onto a glass Petri dish and oven dried at 80 °C overnight. Table 1 reports the initial composition of the inorganic salts mixtures investigated in the present study, and the relative samples coding. Characterisation data concerning both Ni25-Cu75 and Cu100

Table 1
Initial composition of the inorganic salts mixtures.

Sample name	Inorganic salts mixtures (mmol; g)		
	Fe $(NO_3)_3 \cdot 9 H_2O$	Ni $(NO_3)_2 \cdot 6 H_2O$	Cu $(NO_3)_2 \cdot 3 H_2O$
Ni100	10.00; 4.0	5.00; 1.5	-
Ni75-Cu25	10.00; 4.0	3.75; 1.1	1.25; 0.3
Ni50-Cu50	10.00; 4.0	2.50; 0.7	2.50; 0.6
Ni25-Cu75	10.00; 4.0	1.25; 0.4	3.75; 0.9
Cu100	10.00; 4.0	-	5.00; 1.2

are reported in the Supplementary Materials (Fig. S1-S3, *vide infra*).

2.3. Characterisations

Scanning electron microscopy (SEM) micrographs were collected by means of a Zeiss Gemini 500 microscope equipped with a traditional electron detector and a Bruker Quantax detector for energy dispersive X-ray spectroscopy (EDS) microanalysis. Samples were deposited onto SEM stubs using a double-adhesive carbon tape for SEM-EDS analysis. Stabs were covered with a gold coating to avoid any charging effects by means of an Edwards S150B sputter coater.

Transmission electron microscopy (TEM) micrographs were collected by means of a JEOL JEM-2100Plus TEM operating with an acceleration voltage of 200 kV with a 0.24 nm point-to-point resolution. Samples were deposited onto carbon coated Cu TEM mesh grids by drop-casting a dilute dispersion of the nanomaterials in acetone.

X-ray powder diffraction (XRD) patterns were recorded by means of a Rigaku Miniflex 600. The acquisition was performed using a Cu source (40 kV, 15 mA), scanning in the 10–70°2θ range, with a step size of 0.02 degrees, and angular velocity 1.0 degrees per minute. Instrumental PDXL-2 software is used for the sake of comparison with reference diffraction patterns from the ICDD database.

The crystallite average size was estimated by means of the Scherrer equation (Eq. (**1**)):

$$\tau = \frac{K\lambda}{\beta\cos\theta}$$

where τ is the average size of the crystalline domains (expressed in nm), K is the shape factor (typically 0.9), λ is the X-ray wavelength (0.154 nm for a Cu source), β is the line broadening at half the maximum intensity (FWHM) of the selected Bragg angle after subtracting the instrumental line broadening (expressed in radians), and θ is the Bragg angle (expressed in radians). For the Ni ferrite systems, the Bragg angle selected is the crystal reflection at *ca.* 2θ = 35.7°, corresponding to the Miller index (311).

The lattice parameters were calculated using the Instrumental PDXL-2 software.

The magnetic characterisation was performed by Magnetometer using a EZ-9 MicroSense Vibrating Sample Magnetometer (VSM), with resolution of 1 μemu and maximum field of 2.25 T. The measurements were performed at RT, with the material contained in quartz cuvettes. The absence of any ferromagnetic contribution from the cuvettes was verified before each measurement, and the intrinsic diamagnetic contribution due to the quartz material was measured on empty cuvettes and automatically subtracted.

Transmission Mössbauer spectroscopy (TMS) was conducted with a commercial Wissel system in constant acceleration mode, at RT, and by making use of a ^{57}Co source embedded in Rh matrix. Samples for TMS were in powder form, and the quantities used were 1.3231 g, 1.3878 g and 1.3131 g for Ni100, Ni75-Cu25 and Ni50-Cu50, respectively.

Fe, Ni and Cu concentrations were determined by inductively coupled plasma - optical emission spectroscopy (*ICP-OES – Optima 7000 DV Perkin Elmer*) equipped with a PEEK Mira Mist nebulizer, a cyclonic spray chamber and an Echelle monochromator. The wavelengths were 238.204 nm (Fe), 231.604 nm (Ni), and 327.393 nm (Cu). Each concentration value was calculated considering the average value of three instrumental measurements. The selected dissolution procedure was an acid digestion carried out in a microwave oven (*Milestone MLS-1200 MEGA*). Three different sample aliquots were treated with 5 mL of aqua regia in tetrafluoromethoxyl (TFM) bombs. Four heating steps of 5 min each (250, 400, 600, 250 W power respectively) were applied, followed by a ventilation step of 25 min. At the end of the entire treatment, the samples appeared completely dissolved. Finally, the resulting solutions were diluted to 25 mL with high-pure water. A further dilution (1:100) was necessary to determine the concentrations of Fe, Ni and Cu

in the three selected samples, namely: Ni100, Ni75-Cu25 and Ni50-Cu50.

3. Results and discussion

3.1. Morphological and structural characterisation

Fig. 1 and Fig. S1 (Supporting Materials) report the SEM and TEM morphological characterisation of Cu-substituted Ni ferrite samples, whereas EDS microanalysis is reported in Fig. S2 (Supporting Materials). In detail, SEM micrographs show that Ni100 sample (Fig. 1A) consists of aggregates of polyhedral particles with average diameters in the *approx.* 50–200 nm range, whereas high resolution TEM micrograph (Fig. 1B) points out the predominance of an octahedral organization [49,51]. The introduction of Cu as doping heteroatom in the synthetic process causes a gradually reduction of the average diameter of the ferrite nanoparticles, with Ni75-Cu25 (Fig. 1C) and Ni50-Cu50 (Fig. 1D) samples showing their average size centred at *ca.* 100 nm and *ca.* 50 nm, respectively, without altering the Ni ferrite original octahedral morphology. Moreover, the presence of both Ni and Cu elements in both Ni75-Cu25 and Ni50-Cu50 samples was confirmed by their relative EDS microanalysis (Fig. S2, Supporting Materials).

Interestingly, in the case of samples at higher content of Cu (*i.e.*, Ni25-Cu75, and Cu100), a remarkable change in their morphologies and structural organizations was registered. In fact, Ni25-Cu75 sample shows an intrinsic heterogeneity, with presence of two distinct morphologies. Some areas of the sample (defined as morphology (a)) are organized as platelet structures partially included within a disordered matrix (Fig. S1A, Supporting Materials). Vice versa, other areas of the Ni25-Cu75 sample (defined as morphology (b)) are organized as homogeneous domains constituted by large grains sintered between each other, whose average size is of several μm (Fig. S1B, Supporting Materials) [52]. In both these cases, the EDS microanalysis revealed the presence of both Fe and O, together with traces of Na (coming from the alkaline environment of the reaction medium), and surprisingly absence of both Ni and Cu (Fig. S2, Supporting Materials). Finally, in the case of Cu100 sample (Fig. S1C, Supporting Materials), it was registered the co-presence of large octahedral particles (in Fig. S1C, Supporting Materials, it is also possible to appreciate the presence of a geminate) and small platelet nanostructures. In the case of Cu100 sample, the EDS microanalysis (Fig. S2, Supporting Materials) is extremely precious as it allows to make a distinction of the elements forming the two nanostructures. In details, octahedral systems registered the presence of Fe, Cu, and O elements, whereas platelet nanostructures registered the presence of only Cu and O, thus indicating a different chemical composition between the two nanostructures.

X-ray diffractograms of Cu-substituted Ni ferrite samples are reported in Fig. 2, and Fig. S3 (Supporting Materials). XRD patterns of Ni-100, Ni75-Cu25, and Ni50-Cu50 samples show the main reflections at 2θ = 18.4° (111), 30.3° (220), 35.7° (311), 37.3° (222), 43.4° (400), 53.8° (422), 57.4° (511), and 63.0° (440), which can be associated to the presence of a Ni ferrite crystal phase (card number 00–054-0964, ICDD, Fig. 2) [53]. This behaviour clearly indicates that the crystal structure of Ni ferrite (as in Ni100) is retained even in the case of the other two Cu-containing samples (Ni75-Cu25, and Ni50-Cu50), and this agrees with the outcomes deriving from the morphological characterisation [54]. In the case of Ni100 sample, a weak single extra peak at *ca.* 2θ = 33.1° has been registered, and this signal can be probably associated to traces of either by-products or hematite (α-Fe$_2$O$_3$) crystal phase (card number 01–089-2810, ICDD, *vide infra*).

Furthermore, XRD results reveal a Ni ferrite structure with a lattice parameter "*a*" of 8.366 Å in the case of Ni100 sample, 8.340 Å in the case of Ni75-Cu25 sample, and 8.358 Å in the case of Ni50-Cu50 sample, all of them larger than the reference one (*i.e.*, 8.337 Å, from 00–054-0964, ICDD), but in line with the literature [55], thus following the order Ni100 > Ni50-Cu50 > Ni75-Cu25 (Table S1, Supporting
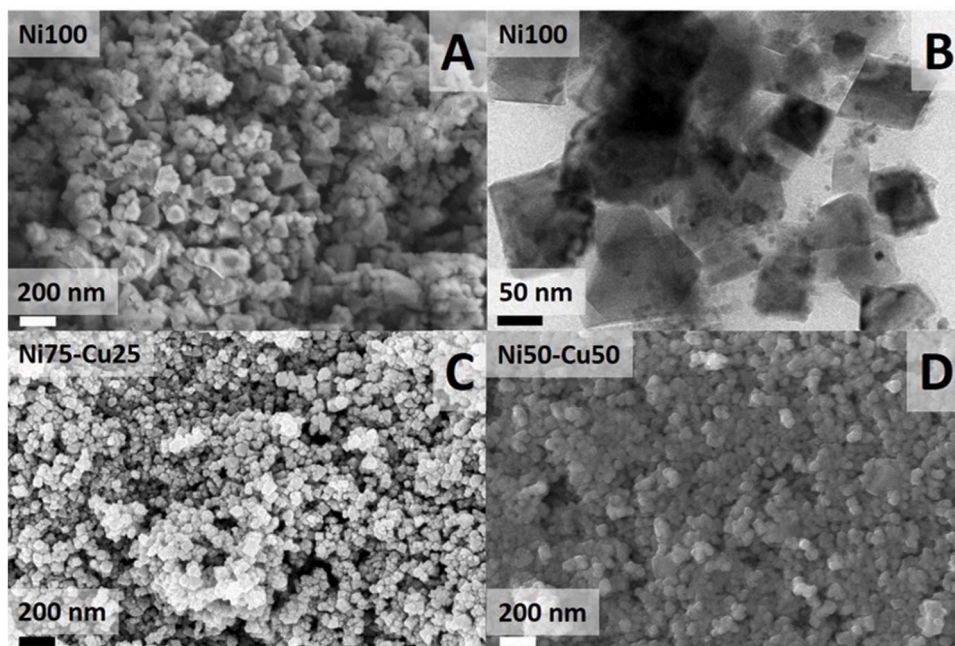
Fig. 1. Morphological characterisation. Panels A, C, and D: SEM micrographs of Ni100 (A, top, left), Ni75-Cu25 (C, bottom, left), and Ni50-Cu50 (D, bottom, right). Panel B: TEM micrograph of Ni100 (B, top, right). All SEM micrographs were collected at the same magnification.
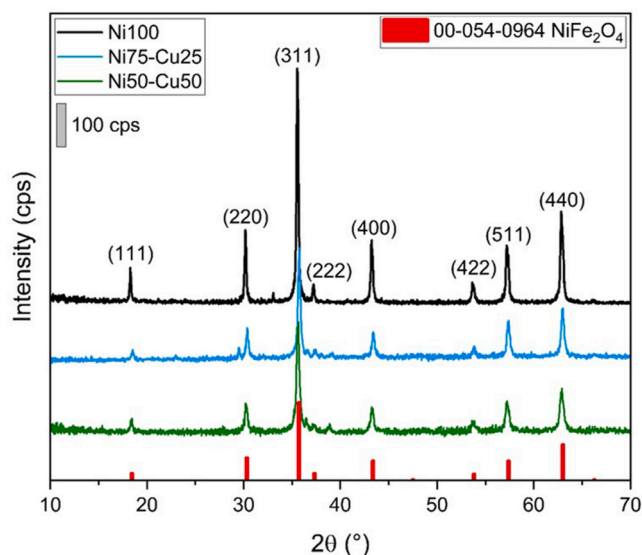

Fig. 2. XRD patterns of Ni100 (black line), Ni75-Cu25 (cyan line), and Ni50-Cu50 (green line). XRD reference pattern: NiFe$_2$O$_4$ (00–054-0964, red).

Materials). Interestingly, the crystallite average size estimated by the Scherrer equation (Eq. (**1**)) decreases with the Cu doping, following the order Ni100 (47 nm) > Ni75-Cu25 (32 nm) > Ni50-Cu50 (26 nm) (Table S1, Supporting Materials).

By further increasing the Cu content in the Ni ferrite samples, it has been evidenced the appearance of different crystal phases associated to the different morphologies registered. In particular, the intrinsic heterogeneity of Ni25-Cu75 sample is confirmed by the presence of the main reflections at $2\theta = 30.1°$ (220), $35.4°$ (311), $43.1°$ (400), $53.4°$ (422), $57.0°$ (333), and $62.6°$ (440), which can be associated to the presence of the magnetite (Fe$_3$O$_4$) crystal phase (card number 01–074-0748, ICDD, Fig. S3A, Supporting Materials) [56], and few weak reflections at $2\theta = 35.5°$ (11−1), $38.7°$ (111), and $48.7°$ (20−2), which can be attributable to traces of tenorite (CuO) crystal phase (card

number 00–048-1548, ICDD, Fig. S3A, Supporting Materials) [57]. This heterogeneity is also in agreement with both the morphological characterisation and the EDS microanalysis. In fact, the platelet structures can be associated to the presence of the tenorite (CuO) phase [58], whereas the rest of the sample is attributable to magnetite grains.

Even the XRD pattern of Cu100 sample is a mixture between two different crystal phases. In fact, Cu100 main reflections at $2\theta = 24.1°$ (012), $33.2°$ (104), $35.6°$ (110), $40.8°$ (113), $49.4°$ (024), $54.0°$ (116), $57.6°$ (018), $62.4°$ (214), and $63.9°$ (300) can be associated to the presence hematite (α-Fe$_2$O$_3$) crystal phase (card number 01–089-2810, ICDD, Fig. S3B, Supporting Materials) [59]. On the contrary, Cu100 reflections at $2\theta = 32.5°$ (110), $35.5°$ (11−1), $38.7°$ (111), $48.7°$ (20−2), $58.3°$ (202), $61.5°$ (11−3), $65.8°$ (022), and $66.2°$ (31−1) are attributable to the presence of tenorite (CuO) crystal phase (card number 00–048-1548, ICDD, Fig. S3B, Supporting Materials) [57]. Even in this case, this behaviour agrees with the experimental evidences coming from the morphological characterisation, as the presence of Fe-containing octahedral systems can be correlated with the presence of hematite (α-Fe$_2$O$_3$) crystal phase [60], whereas platelet Cu-containing nanostructures to the tenorite (CuO) one [58].

Therefore, the morphological and structural characterisation performed on the different Cu-substituted Ni ferrite samples obtained following the selected hydrothermal route evidences the key role played by Cu atoms in the final nanomaterials, as follows:

(1) By partially substituting Ni with Cu, maintaining the nominal degree of Ni substitution with Cu below 50%, the Ni ferrite polyhedral morphology is retained, registering a gradual decrease of the particle size, from *ca.* 200 nm (Ni100) to *ca.* 50 nm (Ni50-Cu50), along with the Cu substitution. The crystal phase of the Ni ferrite is also retained for all samples (*i.e.*, Ni100, Ni75-Cu25, and Ni50-Cu50), however the XRD results reveal a decrease of both the lattice parameter following the order Ni100 > Ni50-Cu50 > Ni75-Cu25, and crystallite average diameters, from 47 nm (Ni100) to 26 nm (Ni50-Cu50).

(2) By substantially replacing Ni with Cu at higher degrees of substitution (*i.e.*, more than 50%), the two systems produced (*i.e.*, Ni25-Cu75, and Cu100) became heterogeneous, with co-presence

of different sub-families of nanoparticles, attributable to CuO and iron oxides (*i.e.,* either magnetite or hematite), and absence of formation of Cu ferrite.

3.2. Magnetic and spectroscopic characterisation

Magnetic properties of Ni100, Ni75-Cu25, and Ni50-Cu50 samples are evaluated by means of M(H) magnetisation curves measured by VSM at RT (Fig. 3), whereas numerical parameters are summarized in Table 2.

All samples basically show superparamagnetic behaviours, as evidenced in the main panel of Fig. 3. The undoped Ni100 sample magnetisation curve, saturating at a value (M_s) of *ca.* 48.5 emu g^{-1}, can be fitted by a Langevin function [61], holding a magnetic moment equal to $\mu = 3.1 \times 10^4$ μB for each particle. A narrow hysteresis loop with magnetic remanence (M_r) of *ca.* 6.1 emu g^{-1}, and an intrinsic coercivity (H_c) of *ca.* 43.5 Oe, are anyway present [62]. The introduction of Cu^{2+} ions within the Ni ferrite structure causes a reduction of the values of M_s following the order: Ni100 (*ca.* 48.5 emu g^{-1}) > Ni50-Cu50 (*ca.* 44.3 emu g^{-1}) > Ni75-Cu25 (*ca.* 40.3 emu g^{-1}), and the disappearance of the hysteresis loop. Interestingly, the Langevin fit gives magnetic moments equal to $\mu = 4.4 \times 10^4$ μB and 4.3×10^4 μB for Ni75-Cu25 and Ni50-Cu50 samples, respectively, thus essentially equivalent and larger than in Ni100 (3.1×10^4 μB). To give a rationale of this trend, transmission Mössbauer spectroscopy (TMS) was performed on these systems.

The TMS spectra of all Cu-substituted Ni ferrite samples (*i.e.*, Ni100, Ni75-Cu25, and Ni50-Cu50) show the presence of two magnetically-split sextets, with an additional small unresolved central (paramagnetic) doublet only for the sample Ni100, which takes up < 10% intensity (Fig. 4). Table 3 summarizes the hyperfine parameters (isomer shift δ, quadrupole splitting Δ, hyperfine magnetic field B_{hf}, and average linewidth Γ), as obtained from the fit of the spectra by using the Vinda software package [63]. The δ are given relative to α-Fe.

By comparing the hyperfine parameters obtained from the fit of Ni100 curve with those known for NiFe$_2$O$_4$ [64], we unambiguously attribute the two sextets to the presence of Fe^{3+} in the local tetrahedral (lower B_{hf}) and octahedral (higher B_{hf}) configurations. By increasing the Cu-dopant concentration, a trend is observed, which is depicted in Fig. 5 (where the x-axis is the relative % of Ni). By adding Cu to the un-doped NiFe$_2$O$_4$ (sample Ni100), we observe a gradual lowering of the Fe^{3+} fraction in the octahedral sites corresponding to an increased fraction of Fe^{3+} occupying the tetrahedral sites (Fig. 5**C**). However, it should be
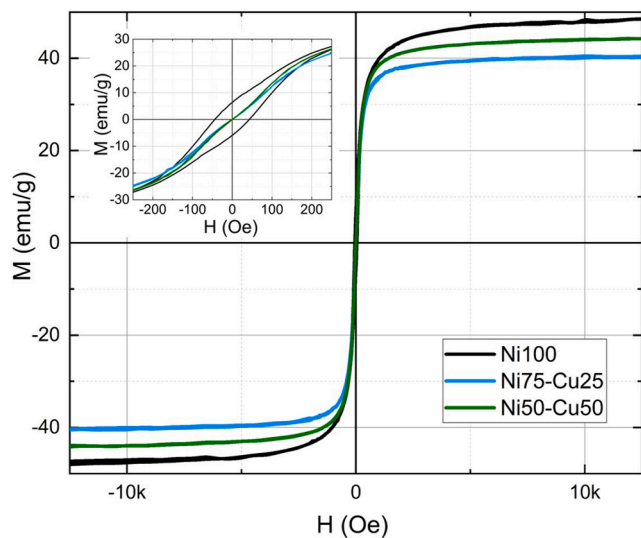

Fig. 3. Magnetisation curves M *vs.* H of Ni100 (black line), Ni75-Cu25 (cyan line), and Ni50-Cu50 (green line). Inset shows the magnetisation curve enlargement in order to highlight the middle section of the hysteresis loop.

Table 2
Magnetic properties of Cu-substituted Ni ferrite samples measured at RT.

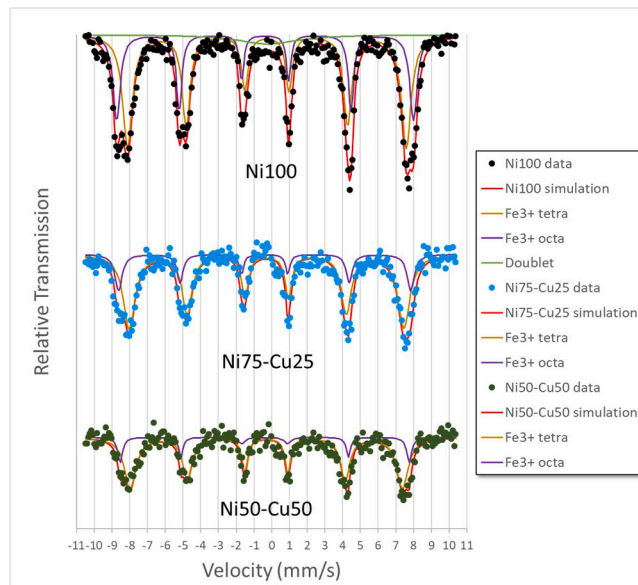| Sample name	M_s (emu g^{-1})	M_r (emu g^{-1})	H_c (Oe)
Ni100	48.5	6.1	43.5
Ni75-Cu25	40.3	0.0	0.0
Ni50-Cu50	44.3	0.0	0.0

Fig. 4. TMS spectra obtained at RT for the Ni100 (top), Ni75-Cu25 (middle) and Ni50-Cu50 (bottom) samples.

Table 3
Hyperfine parameters (isomer shift δ, quadrupole splitting Δ, hyperfine magnetic field B_{hf}, and average linewidth Γ) obtained from the fit of the TMS spectra of samples Ni100, Ni75-Cu25 and Ni50-Cu50. The relative spectral area (%) is also indicated, by assuming an identical recoilless factor equal to 1.

Ni100	δ (mm s^{-1})	Δ (mm s^{-1})	B_{hf} (T)	Γ (mm s^{-1})	%
Fe^{3+} tetra	0.270(4)	0	48.63(3)	0.56(4)	59(1)
Fe^{3+} octa	0.372(4)	0	51.80(3)	0.39(3)	33(1)
Ni75-Cu25	δ (mm s^{-1})	Δ (mm s^{-1})	B_{hf} (T)	Γ (mm s^{-1})	%
Fe^{3+} tetra	0.284(5)	0	47.93(6)	0.65(6)	77(1)
Fe^{3+} octa	0.397(9)	0	51.0(1)	0.40(9)	23(1)
Ni50-Cu50	δ (mm s^{-1})	Δ (mm s^{-1})	B_{hf} (T)	Γ (mm s^{-1})	%
Fe^{3+} tetra	0.304(7)	0	47.53(9)	0.60(9)	83(1)
Fe^{3+} octa	0.39(1)	0	50.44(9)	0.4(1)	17(1)

pointed out that while VSM probes the volume-magnetic behaviour of the samples, TMS probes the local hyperfine magnetic field at separate Fe sites (both tetrahedral and octahedral sites). TMS shows a gradual lowering of the B_{hf} at both tetrahedral and octahedral sites by increasing Cu content (Fig. 5B), while VSM observes a higher M_s value for the Ni50-Cu50 sample compared to the Ni75-Cu25 sample, thus suggesting a possible stronger intergrain magnetic coupling in the Ni50-Cu50 case, to which TMS is not sensitive. In the stoichiometric NiFe$_2$O$_4$ (Ni100 sample), the macroscopic magnetisation only comes from the Ni^{2+} ions at the octahedral sites, since the Fe^{3+} ions in the tetrahedral and octahedral sites contribute equally but with opposite magnetic moments, thus providing an overall null contribution to the magnetisation [65]. According to the study by Kumar *et al.* [54] regarding analogous Cu-substituted Ni ferrite systems, the introduction of Cu^{2+} at the expenses of Ni^{2+} causes a partial replacement of Fe^{3+} atoms from the tetrahedral A-sites by means of Cu^{2+} ions, with migration of Fe^{3+} ions
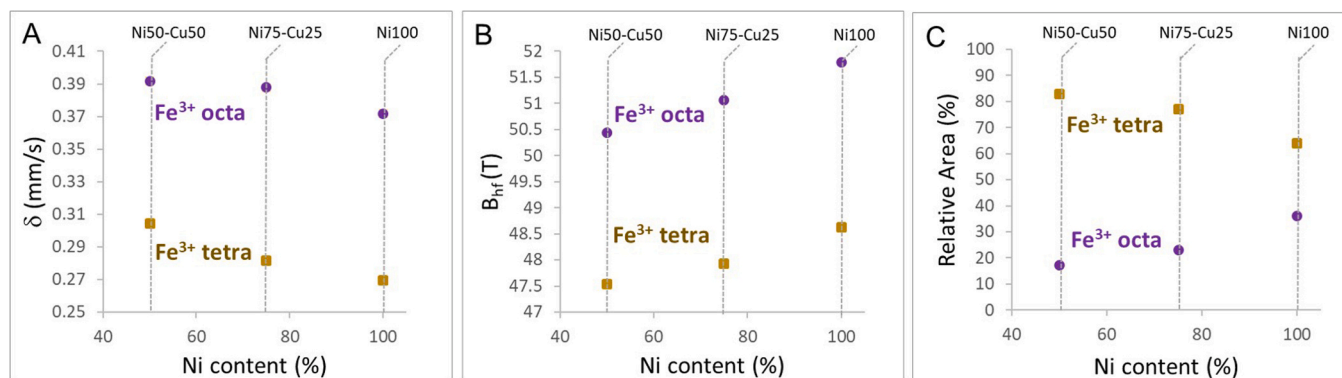
Fig. 5. Cu-concentration dependence of the (a) isomer shift, (b) hyperfine magnetic field, and (c) relative spectral area, as obtained following the fit of the TMS spectra shown in Fig. 4, as a function of the Ni concentration. The area fraction for Ni100 was normalized to the total magnetic fraction (octahedral and tetrahedral contribution).

from the tetrahedral A-sites to the octahedral B-sites. This phenomenon causes an increment of the Fe^{3+} concentration in the octahedral B-sites, and consequently an increase of the magnetic moment contribution due to the B-sites. Furthermore, the substitution of Fe^{3+} ions with Cu^{2+} ones in the A-sites causes a further reduction of the magnetic moment contribution due to the A-sites. The overall contribution of both A-sites and B-sites corresponds to an increment of the magnetisation, following the order from bare $NiFe_2O_4$ to $Ni_{0.5}Cu_{0.5}Fe_2O_4$. Even Rais *et al.* [40] reported that the substitution of Ni^{2+} with Cu^{2+} in Ni ferrites causes a preferential replacement of the Fe^{3+} ions (0.67 Å) from the tetrahedral A-sites with the larger Cu^{2+} ions (0.72 Å), and the consequent replacement of Ni^{2+} ions (0.69 Å) with the smaller Fe^{3+} ones within the octahedral B-sites. On the contrary, Al-Rawas *et al.* [41] reported the preferential tendency of Cu^{2+} ions to occupy the octahedral B-sites.

In our case, the TMS data confirm that the increment of Cu^{2+} ions causes a progressively reduction of the contribution due to Fe^{3+} ions at the octahedral B-sites, with a tendency of Fe^{3+} of preferentially occupying the tetrahedral A-sites. This datum suggests that Cu^{2+} ions probably tend to occupy the octahedral B-sites rather than the tetrahedral A-sites. This hypothesis is also in agreement with the magnetic characterisation. In fact, if the introduction of Cu^{2+} ions in the Ni ferrite structure leaves almost unaltered the composition of the tetrahedral A-sites (occupied primarily by Fe^{3+} ions), the progressively replacement of both Ni^{2+} and Fe^{3+} ions at the octahedral B-sites with Cu^{2+} ions causes an overall decrease of the magnetisation saturation. Furthermore, the nonlinear trend existing between magnetisation *vs.* Cu content experimentally registered in our study, with higher M_s value for Ni50-Cu50 (*ca.* 44.3 emu g^{-1}) sample compared to that of Ni75-Cu25 (*ca.* 40.3 emu g^{-1}) sample, can be partially explained by considering the literature. In particular, Gabal *et al.* [66] registered a decrease of the M_s value from bare Ni ferrite to the Cu-Ni mixed ferrite with 0.3 of Cu molar content, followed by a slight increment at 0.5 of Cu content, and attributed this phenomenon to the cation distribution and Neel's model. However, it should be also considered the possibility that by increasing the concentration of Cu^{2+} ions, it is possible that they can partially substitute Fe^{3+} species even in the tetrahedral A-sites, thus causing also a decrease of the magnetic moment contribution due to the A-sites, giving an overall slight increment of the magnetisation [54]. Even Jnaneshwara *et al.* [67] registered a decrease of the coercivity values by increasing the Cu content, and attributed this phenomenon to the small magnetic anisotropy of Cu^{2+} ions.

In order to give a rationale to the data here obtained, at least in the case of the stoichiometric Ni100 sample, the main contribution to the M_s is given by the presence of the Ni^{2+} ions occupying the octahedral B-sites (as the Fe^{3+} ions contribution is null since they stoichiometrically occupy both tetrahedral A-sites and octahedral B-sites), whereas the coercivity value and the presence of an hysteresis registered for the

Ni100 sample can be explained considering the different particle size/domain structure of this sample [68,69]. According to the TMS analysis and the magnetisation curves, the introduction of Cu^{2+} in the Ni ferrite structure surely causes a reduction of the Fe^{3+} ions contribution at the octahedral B-sites and a consequent M_s reduction. In principle, both these evidences could be potentially associated to a gradual occupation of the octahedral B-sites by the Cu^{2+} ions, but this is a speculation as with TMS analysis it is possible to monitor only the fate of iron atoms, and not the fate of copper ones. However, this last assumption is also consistent with the results by Dey *et al.* [70], where the authors reported that in analogous systems constituted by Cu-doped Ni ferrites, Cu ions preferentially occupied the octahedral B-sites meanwhile some of them occupied also the tetrahedral A-sites, thus consequently Fe ions migrated to the octahedral B-sites for maintaining the charge equilibrium and chemical composition stoichiometry. A decrease of the magnetisation saturation with the Cu-doping in Ni ferrite has also been registered by Sukumar *et al.* [71], and authors attributed such decrement to different factors, such as: lattice defects, random magnetic, magnetic super exchange interactions, cationic redistribution, and orientation of spins.

For completeness, the metal composition of Cu-Ni ferrite samples (namely, Ni100, Ni75-Cu25, and Ni50-Cu50) has been measured by means of ICP-OES. Numerical values reported in Table 4 confirm the gradual reduction of the Ni content within the ferrite samples following the order Ni100 > Ni75-Cu25 > Ni50-Cu50, coupled with the increment of Cu content following the opposite order Ni50-Cu50 > Ni75-Cu25 > > Ni100 (*i.e.*, in this last case, obviously, Cu is absent). What is interesting, is the behaviour of iron which follows the order Ni100 > Ni50-Cu50 > Ni75-Cu25, thus suggesting that the Ni75-Cu25 sample has less Fe content than both Ni100 and Ni50-Cu50 samples. Interestingly, this trend is also in agreement with the decrease of the lattice parameter registered for the three samples analysed. This particular behaviour could be associated with the influence of Cu^{2+} substitution in the Ni ferrite structure, with a preferential replacement of Fe^{3+} from the octahedral B-sites toward the tetrahedral A-sites. Additionally, by considering the sum of the contribution of the chemical elements able in providing a magnetic response (*i.e.*, both Fe and Ni) for the three ferrites samples here considered, it follows the order: Ni100 > Ni50-Cu50 > Ni75-Cu25, still in agreement with the M_s trend

Table 4
Fe, Ni and Cu concentrations determined by means of ICP-OES (data are expressed as g kg^{-1} ± SD).

Samples name	Fe (g kg^{-1})	Ni (g kg^{-1})	Cu (g kg^{-1})
Ni100	448 ± 17	223 ± 8	< 2
Ni75-Cu25	354 ± 22	134 ± 9	58 ± 4
Ni50-Cu50	426 ± 18	102 ± 5	111 ± 5

reported in Table 2.

4. Conclusions

The present study focuses on the effect of Cu-substitution into Ni ferrite systems produced following a hydrothermal route carried out at relatively mild conditions, namely at temperature below 200 °C. Different degrees of substitution were investigated, ranging from bare Ni ferrite to a complete Cu-substituted system (by replacing 100% of Ni with Cu). Morphological and structural characterisation points out that the introduction of Cu in the Ni ferrite causes a gradual reduction of the average diameters of the ferrite polyhedral nanoparticles, from *approx.* 200 nm in the case of Ni100 sample (bare Ni ferrite), to 50 nm in the case of ferrite with nominal 50% substitution (Ni50-Cu50), without altering the Ni ferrite crystal phase, but revealing a decrease of both the lattice parameter following the order Ni100 > Ni50-Cu50 > Ni75-Cu25, and crystallite average diameters, from 47 nm (Ni100) to 26 nm (Ni50-Cu50).

At higher content of Cu (75%–100% Ni substitution), instead, the morphology evolves toward a heterogeneous system registering the co-presence of the different oxides, namely hematite/magnetite and tenorite, and absence of Cu ferrite phase.

Magnetic properties of Ni100, Ni75-Cu25, and Ni50-Cu50 samples evidence that all samples are mostly superparamagnetic. The introduction of Cu^{2+} ions in the Ni ferrite causes a reduction of the values of magnetisation saturation, and the disappearance of the hysteresis loop. Transmission Mössbauer spectroscopy performed on these samples evidences the presence of Fe in the local tetrahedral and octahedral configurations. By increasing the Cu-dopant concentration, a gradual lowering of the Fe fraction in the octahedral sites is observed corresponding to an increment of the Fe fraction in the tetrahedral A-sites. Lastly, the metal composition of Cu-Ni ferrite samples has been measured by means of ICP-OES, confirming the gradual reduction of the Ni content within ferrite samples following the order Ni100 > Ni75-Cu25 > Ni50-Cu50, coupled with the increment of Cu content following the opposite order Ni50-Cu50 > Ni75-Cu25 > > Ni100. Interestingly, the Fe content follows the order Ni100 > Ni50-Cu50 > Ni75-Cu25, thus suggesting that the Ni75-Cu25 sample has less Fe content than both Ni100 and Ni50-Cu50 samples. This particular behaviour could be associated with the influence of Cu substitution in the Ni ferrite structure, with preferential replacement of Fe from the octahedral B-sites toward the tetrahedral A-sites.

CRediT authorship contribution statement

Mostoni Silvia: Data curation, Methodology, Writing – review & editing. **D'Arienzo Massimiliano:** Writing – review & editing. **Di Credico Barbara:** Writing – review & editing. **Scotti Roberto:** Writing – review & editing. **Nisticò Roberto:** Conceptualization, Data curation, Methodology, Supervision, Writing – original draft, Writing – review & editing. **Mantovan Roberto:** Data curation, Methodology, Writing – original draft, Writing – review & editing. **Cantoni Matteo:** Data curation, Methodology, Writing – original draft, Writing – review & editing. **Rinaldi Christian:** Data curation, Methodology, Writing – review & editing. **Malandrino Mery:** Data curation, Methodology, Writing – review & editing.

Declaration of Competing Interest

The authors declare that they have no known competing financial interests or personal relationships that could have appeared to influence the work reported in this paper.

Data Availability

Data will be made available on request.

Appendix A. Supporting information

Supplementary data associated with this article can be found in the online version at doi:10.1016/j.jallcom.2024.173628.

References

[1] D. Yan, Z. Wang, Z. Zhang, Stimuli-responsive crystalline smart materials: from rational design and fabrication to applications, Acc. Chem. Res. 55 (2022) 1047–1058, https://doi.org/10.1021/acs.accounts.2c00027.

[2] A. Dzubinska, M. Giovannini, M. Reiffers, J. Rodriguez-Fernandez, J.I. Espeso, I. Curlik, K. Arun, R. Varga, J.C. Gomez Sal, Crystallographic, magnetic and magnetocaloric properties in Yb-based alloy, J. Magn. Magn. Mater. 551 (2022) 169102, https://doi.org/10.1016/j.jmmm.2022.169102.

[3] H. Lin, J. Yang, H. Zhao, J. Gou, Y. Zhang, J. Fu, F. Sun, W. Ruan, Z. Zhang, X. Liang, S. Ren, T. Ma, J. Ma, J. Shen, Fabrication of magnetostrictive composites using metallic glass as glue, Intermetallics 145 (2022) 107561, https://doi.org/10.1016/j.intermet.2022.107561.

[4] Y. Zhang, J. Li, P. Habibovic, Magnetically responsive nanofibrous ceramic scaffolds for on-demand motion and drug delivery, Bioact. Mater. 15 (2022) 372–381, https://doi.org/10.1016/j.bioactmat.2022.02.028.

[5] S. Namathoti, R. Kumar V.M, R. Sreekanth P.S, A review on progress in magnetic, microwave, ultrasonic responsive shape-memory polymer composites, Mater. Today Proc. 56 (2022) 1182–1191, https://doi.org/10.1016/j.matpr.2021.11.151.

[6] J. Lu, W. Zhu, L. Dai, C. Si, Y. Ni, Fabrication of thermo- and pH-sensitive cellulose nanofibrils-reinforced hydrogel with biomass nanoparticles, Carbohydr. Polym. 215 (2019) 289–295, https://doi.org/10.1016/j.carbpol.2019.03.100.

[7] S.A. Jadhav, R. Nisticò, G. Magnacca, D. Scalarone, Packed hybrid silica nanoparticles as sorbents with thermo-switchable surface chemistry and pore size for fast extraction of environmental pollutants, RSC Adv. 8 (2018) 1246–1254, https://doi.org/10.1039/c7ra11869d.

[8] A. Abdollahi, H. Roghani-Mamaqani, B. Razavi, Stimuli-chromism of photoswitches in smart polymers: Recent advances and applications as chemosensors, Progr. Polym. Sci. 98 (2019) 101149, https://doi.org/10.1016/j.progpolymsci.2019.101149.

[9] C. Yin, L. Dong, Z. Wang, M. Chen, Y. Wang, Y. Zhao, CO_2-responsive graphene oxide nanofiltration membranes for switchable rejection to cations and anions, J. Membr. Sci. 592 (2019) 117374, https://doi.org/10.1016/j.memsci.2019.117374.

[10] W. Wang, M. Zhou, Degradation of trichloroethylene using solvent-responsive polymer coated Fe nanoparticles, Colloids Surf. A Physicochem. Eng. Asp. 369 (2010) 232–239, https://doi.org/10.1016/j.colsurfa.2010.08.031.

[11] K.K. Patel, R. Purohit, Improved shape memory and mechanical properties of microwave-induced shape memory polymer/MWCNTs composites, Mater. Today Comm. 20 (2019) 100579, https://doi.org/10.1016/j.mtcomm.2019.100579.

[12] J. Kolosnjaj-Tabi, L. Gibot, I. Fourquaux, M. Golzio, M.-P. Rols, Electric field-responsive nanoparticles and electric fields: physical, chemical, biological mechanisms and therapeutic prospects, Adv. Drug Deliv. Rev. 138 (2019) 56, https://doi.org/10.1016/j.addr.2018.10.017.

[13] R. Nisticò, A synthetic guide toward the tailored production of magnetic iron oxide nanoparticles, Bol. Soc. Esp. Ceram. V. 60 (2021) 29–40, https://doi.org/10.1016/j.bsecv.2020.01.011.

[14] R. Nisticò, F. Cesano, F. Garello, Magnetic materials and systems: domain structure visualization and other characterization techniques for the application in the materials science and biomedicine, Inorganics 8 (2020) 6, https://doi.org/10.3390/inorganics8010006.

[15] S. Amiri, H. Shokrollahi, The role of cobalt ferrite magnetic nanoparticles in medical science, Mater. Sci. Eng. C. 33 (2013) 1–8, https://doi.org/10.1016/j.msec.2012.09.003.

[16] K.E. Peyer, L. Zhang, B.J. Nelson, Bio-inspired magnetic swimming microrobots for biomedical applications, Nanoscale 5 (2013) 1259–1272, https://doi.org/10.1039/C2NR33254C.

[17] D. Giraldo, P. Almodovar, M.L. Lopez, E. Rodriguez-Aguado, E. Rodriguez-Castellon, A. Galdamez, I. Alvarez-Serrano, Exploring multiferroicity in $BiFeO_3$ – $NaNbO_3$ thermistor electroceramics, J. Eur. Ceram. Soc. 41 (2021) 7069–7076, https://doi.org/10.1016/j.jeurceramsoc.2021.07.045.

[18] M. Pooladi, I. Sharifi, M. Behzadipour, A review of the structure, magnetic and electrical properties of bismuth ferrites ($Bi_2Fe_4O_9$), Ceram. Int. 46 (2020) 18453–18463, https://doi.org/10.1016/j.ceramint.2020.04.241.

[19] J. Li, E.S. Barjuei, G. Ciuti, Y. Hao, P. Zhang, A. Menciassi, Q. Huang, P. Dario, Magnetically-driven medical robots: An analytical magnetic model for endoscopic capsules design, J. Magn. Magn. Mater. 452 (2018) 278–287, https://doi.org/10.1016/j.jmmm.2017.12.085.

[20] A.I. Ivanets, V. Srivastava, M.Y. Roshchina, M. Sillampaa, V.G. Prozorovich, V. V. Pankov, Magnesium ferrite nanoparticles as a magnetic sorbent for the removal of Mn^{2+}, Co^{2+}, Ni^{2+} and Cu^{2+} from aqueous solution, Ceram. Int. 44 (2018) 9097–9104, https://doi.org/10.1016/j.ceramint.2018.02.117.

[21] A.G. Leonel, A.A.P. Mansur, H.S. Mansur, Advanced functional nanostructures based on magnetic iron oxide nanomaterials for water remediation: A review, Water Res 190 (2021) 116693, https://doi.org/10.1016/j.watres.2020.116693.

[22] V. Polliotto, F.R. Pomilla, V. Maurino, G. Marcì, A. Bianco Prevot, R. Nisticò, G. Magnacca, M.C. Paganini, L. Ponce Robles, L. Perez, S. Malato, Different approaches for the solar photocatalytic removal of micro-contaminants from aqueous environment: titania vs. hybrid magnetic iron oxides, Catal. Today 328 (2019) 164–171, https://doi.org/10.1016/j.cattod.2019.01.044.

[23] D. Palma, A. Bianco Prevot, M. Brigante, D. Fabbri, G. Magnacca, C. Richard, G. Mailhot, R. Nisticò, New insights on the photodegradation of caffeine in the presence of bio-based substances-magnetic iron oxide hybrid nanomaterials, Materials 11 (2018) 1084, https://doi.org/10.3390/ma11071084.

[24] M.E. Peralta, S. Ocampo, I.G. Funes, F.O. Medina, M.E. Parolo, L. Carlos, Nanomaterials with tailored magnetic properties as adsorbents of organic pollutants from wastewaters, Inorganics 8 (2020) 24, https://doi.org/10.3390/inorganics8040024.

[25] M.R. Nielsen, A.B. Moss, A.S. Bjornlund, X. Liu, A. Knop-Gericke, A.Y. Klyushin, J.-D. Grunwaldt, T.L. Sheppard, D.E. Doronkin, A. Zimina, T.E.L. Smitshuysen, C. D. Damsgaard, J.B. Wagner, T.W. Hansen, Reduction and carburization of iron oxides for Fischer-Tropsch synthesis, J. Energy Chem. 51 (2020) 48–61, https://doi.org/10.1016/j.jechem.2020.03.026.

[26] M.S. Ansari, M.H.D. Othman, M.O. Ansari, S. Ansari, H. Abdullah, Progress in Fe_3O_4-centered spintronic systems: Development, architecture, and features, Appl. Mater. Today 25 (2021) 101181, https://doi.org/10.1016/j.apmt.2021.101181.

[27] R. Nisticò, Magnetic materials and water treatments for a sustainable future, Res. Chem. Intermed. 43 (2017) 6911–6949, https://doi.org/10.1007/s11164-017-3029-x.

[28] P. Quarterman, C. Sun, J. Garcia-Barriocanal, M. DC, Y. Lv, S. Manipatruni, D. E. Nikonov, I.A. Young, P.M. Voyles, J.-P. Wang, Demonstration of Ru as the 4th ferromagnetic element at room temperature, Nat. Comm. 9 (2018) 2058, https://doi.org/10.1038/s41467-018-04512-1.

[29] S. Gabani, K. Flachbart, K. Siemensmeyer, T. Mori, Magnetism and superconductivity of rare earth borides, J. Alloy. Compd. 821 (2020) 153201, https://doi.org/10.1016/j.jallcom.2019.153201.

[30] A. Namai, M. Yoshikiyo, K. Yamada, S. Sakurai, T. Goto, T. Yoshida, T. Miyazaki, M. Nakajima, T. Suemoto, H. Tokoro, S.-I. Ohkoshi, Hard magnetic ferrite with a gigantic coercivity and high frequency millimeter wave rotation. Nat. Comm. 3 (2012) 1035 https://doi.org/10.1038/ncomms2038.

[31] J.H. Kim, H.E. Kim, J.H. Kim, J.S. Lee, Ferrites: emerging light absorbers for solar water splitting, J. Mater. Chem. A 8 (2020) 9447–9482, https://doi.org/10.1039/D0TA01554G.

[32] J. Wang, Q. Deng, M. Li, K. Jiang, J. Zhang, Z. Hu, J. Chu, Copper ferrites@reduced graphene oxide anode materials for advanced lithium storage applications, Sci. Rep. 7 (2017) 8903, https://doi.org/10.1038/s41598-017-09214-0.

[33] E. Casbeer, V.K. Sharma, X.-Z. Li, Synthesis and photocatalytic activity of ferrites under visible light: a review, Sep. Purif. Technol. 87 (2012) 1–14, https://doi.org/10.1016/j.seppur.2011.11.034.

[34] D. Hong, Y. Yamada, T. Nagatomi, Y. Takai, S. Fukuzumi, Catalysis of nickel ferrite for photocatalytic water oxidation using $[Ru(bpy)_3]^{2+}$ and $S_2O_8^{-}$, J. Am. Chem. Soc. 134 (2012) 19572–19575, https://doi.org/10.1021/ja309771h.

[35] J. Huang, Y. Fu, Y. Zhao, J. Zhang, S. Li, S. Li, G. Li, Z. Chen, Y. Sun, Anti-sintering non-stoichiometric nickel ferrite for highly efficient and thermal-stable thermochemical CO_2 splitting, Chem. Eng. J. 404 (2021) 127067, https://doi.org/10.1016/j.cej.2020.127067.

[36] K. Malaie, Z. Heydari, M.R. Ganjali, Spinel nano-ferrites as low-cost (photo) electrocatalysts with unique electronic properties in solar energy conversion systems, Int. J. Hydrog. Energy 46 (2021) 3510–3529, https://doi.org/10.1016/j.ijhydene.2020.11.009.

[37] W. Ponhan, S. Maensiri, Fabrication and magnetic properties of electrospun copper ferrite ($CuFe_2O_4$) nanofibers, Solid State Sci. 11 (2009) 479–484, https://doi.org/10.1016/j.solidstatesciences.2008.06.019.

[38] P. Chamoli, R.K. Shukla, A.N. Bezbaruah, K.K. Kar, K.K. Raina, Ferrites for water purification and wastewater treatment, in: G.K. Bhargava, S. Bhardwaj, M. Singh, K.M. Batoo (Eds.), Ferrites and Multiferroics. Engineering Materials book series, Springer, (Singapore), 2021, pp. 117–127, https://doi.org/10.1007/978-981-16-7454-9_7.

[39] S.B. Narang, K. Pubby, Nickel spinel ferrites: a review, J. Magn. Magn. Mater. 519 (2021) 167163, https://doi.org/10.1016/j.jmmm.2020.167163.

[40] A. Rais, K. Taibi, A. Addou, A. Zanoun, Y. Al-Douri, Copper substitution effect on the structural properties of nickel ferrites, Ceram. Int. 40 (2014) 14413–14419, 0.1016/j.ceramint.2014.06.037.

[41] A.D. Al-Rawas, A. Rais, A.A. Yousif, A.M. Gismelseed, M.E. Elzain, S. Mazen, A. Al-Falaky, Magnetic properties of $Cu_{1+x}M_xFe_{2-2x}O_4$ mixed ferrites (M=Ge, Ti, $0 \le x \le 0.4$), J. Magn. Magn. Mater. 269 (2004) 168–175, https://doi.org/10.1016/S0304-8853(03)00588-2.

[42] A.P.G. Rodrigues, D.K.S. Gomes, J.H. Araujo, D.M.A. Melo, N.A.S. Oliveira, R. M. Braga, Nanoferrites of nickel doped with cobalt: Influence of Co^{2+} on the structural and magnetic properties, J. Magn. Magn. Mater. 374 (2015) 748–754, https://doi.org/10.1016/j.jmmm.2014.09.045.

[43] S. Diodati, R.I. Walton, S. Mascotto, S. Gross, Low-temperature wet chemistry synthetic approaches towards ferrites, Inorg. Chem. Front. 7 (2020) 3282–3314, https://doi.org/10.1039/D0QI00294A.

[44] M.N. Ashiq, M.F. Ehsan, M.J. Iqbal, I.H. Gul, Synthesis, structural and electrical characterization of Sb^{3+} substituted spinel nickel ferrite ($NiSb_xFe_{2-x}O_4$) nanoparticles by reverse micelle technique, J. Alloy. Compd. 509 (2011) 5119–5126, https://doi.org/10.1016/j.jallcom.2011.01.193.

[45] A. Lakshman, P.S.V.Subba Rao, B.Parvatheeswara Rao, K.H. Rao, Electrical properties of In^{3+} and Cr^{3+} substituted magnesium-manganese ferrites, J. Phys. D: Appl. Phys. 38 (2005) 673, https://doi.org/10.1088/0022-3727/38/5/002.

[46] J. Yu, Y. Hai, M. Jaroniec, Photocatalytic hydrogen production over CuO-modified titania, J. Colloid Interface Sci. 357 (2011) 223–228, https://doi.org/10.1016/j.jcis.2011.01.101.

[47] U. Kang, S.K. Choi, D.J. Ham, S.M. Ji, W. Choi, D.S. Han, A. Abdel-Wahab, H. Park, Photosynthesis of formate from CO_2 and water at 1% energy efficiency via copper iron oxide catalysis, Energy Environ. Sci. 8 (2015) 2638–2643, https://doi.org/10.1039/C5EE01410G.

[48] M.M. Khalaf, H.M. Abd El-Lateef, A.O. Alnajjar, I.M.A. Mohamed, A facile chemical synthesis of $Cu_xNi_{(1-x)}Fe_2O_4$ nanoparticles as a nonprecious ferrite material for electrocatalytic oxidation of acetaldehyde, Sci. Rep. 10 (2020) 2761, https://doi.org/10.1038/s41598-020-59655-3.

[49] M. Dhiman, R. Sharma, V. Kumar, S. Singhal, Morphology controlled hydrothermal synthesis and photocatalytic properties of $ZnFe_2O_4$ nanostructures, Ceram. Int 42 (2016) 12594–12605, https://doi.org/10.1016/j.ceramint.2016.04.115.

[50] M.E. Peralta, R. Nisticò, F. Franzoso, G. Magnacca, L. Fernandez, M.E. Parolo, E. G. Leon, L. Carlos, Highly efficient removal of heavy metals from waters by magnetic chitosan-based composite, Adsorption 25 (2019) 1337–1347, https://doi.org/10.1007/s10450-019-00096-4.

[51] M.K. Shobana, H. Choe, Structural and electrical properties of Cr doped nickel ferrite, J. Mater. Sci. Mater. Electron. 27 (2016) 13052–13056, https://doi.org/10.1007/s10854-016-5446-9.

[52] I.R. Ibrahim, M. Hashim, R. Nazlan, I. Ismail, W.N.W.A. Rahman, N.H. Abdullah, F. M. Idris, M.S.E. Shafie, M.M.M. Zulkimi, Grouping trends of magnetic permeability components in their parallel evolution with microstructure in $Ni_{0.3}Zn_{0.7}Fe_2O_4$, J. Magn. Magn. Mater. 355 (2014) 265–275, https://doi.org/10.1016/j.jmmm.2013.12.024.

[53] R. Thejas, T.L. Soundarya, G. Nagaraju, K. Swaroop, S.C. Prashantha, M. Veena, E. Malagiriyappa, C.S. Naveen, Effect of cation concentration on structural, morphology, optical properties of Zinc-Nickel ferrite nanoparticles, Mater. Lett. X 15 (2022) 100156, https://doi.org/10.1016/j.mlblux.2022.100156.

[54] G.R. Kumar, K.V. Kumar, Y.C. Venudhar, Synthesis, structural and magnetic properties of copper substituted Nickel ferrites by sol-gel method, Mater. Sci. Appl. 3 (2012) 87–91, https://doi.org/10.4236/msa.2012.32013.

[55] C. Sedrati, S. Alleg, H. Boussafel, A.B. Hacine, Structure and magnetic properties of nickel ferrites synthesized by a facile co-precipitation method: effect of the Fe/Ni ratio, J. Mater. Sci.: Mater. Electron. 32 (2021) 24548–24559, https://doi.org/10.1007/s10854-021-06932-0.

[56] R. Nisticò, F. Franzoso, F. Cesano, D. Scarano, G. Magnacca, M.E. Parolo, L. Carlos, Chitosan-derived iron oxide systems for magnetically guided and efficient water purification processes from polycyclic aromatic hydrocarbons, ACS Sustain. Chem. Eng. 5 (2017) 793–801, https://doi.org/10.1021/acssuschemeng.6b02126.

[57] S.P. Meshram, P.V. Adhyapak, U.P. Mulik, D.P. Amalnerkar, Facile synthesis of CuO nanomorphs and their morphology dependent sunlight driven photocatalytic properties, Chem. Eng. J. 204-206 (2012) 158–168, https://doi.org/10.1016/j.cej.2012.07.012.

[58] M. Outokesh, M. Hosseinpour, S.J. Ahmadi, T. Mousavand, S. Sadjadi, W. Soltanian, Hydrothermal synthesis of CuO nanoparticles: Study on effects of operational conditions on yield, purity, and size of the nanoparticles, Ind. Eng. Chem. Res. 50 (2011) 3540–3554, https://doi.org/10.1021/ie1017089.

[59] L. Demarchis, M. Minella, R. Nisticò, V. Maurino, C. Minero, D. Vione, Photo-Fenton reaction in the presence of morphologically controlled hematite as iron source, J. Photochem. Photobiol. A Chem. 397 (2015) 99–107, 0.1016/j.jphotochem.2015.04.009.

[60] N. Sankova, E. Parkhomchuk, Pseudomorphism and size stabilization of hematite particles in the organic phase synthesis, J. Solid State Chem. 282 (2020) 121130, https://doi.org/10.1016/j.jssc.2019.121130.

[61] D. Henrard, Q.L. Vuong, S. Delangre, X. Valentini, D. Nonclercq, M.F. Gonon, Y. Gossuin, Monitoring of superparamagnetic particle sizes in the Langevin law regime, J. Nanomater. 2019 (2019) 6409210, https://doi.org/10.1155/2019/6409210.

[62] T. Ishizaki, K. Yatsugi, K. Akedo, Effect of particle size on the magnetic properties of Ni nanoparticles synthesized with trioctylphosphine as the capping agent, Nanomaterials 6 (2016) 172, https://doi.org/10.3390/nano6090172.

[63] H.P. Gunnlaugsson, Spreadsheet based analysis of Mossbauer spectra, Hyperfine Inter. 237 (2016) 79, https://doi.org/10.1007/s10751-016-1271-z.

[64] V. Sepelak, D. Baabe, D. Mienert, D. Schultze, F. Krumeich, F.J. Litterst, K. D. Becker, Evolution of structure and magnetic properties with annealing temperature in nanoscale high-energy-milled nickel ferrite, J. Magn. Magn. Mater. 257 (2003) 377–386, https://doi.org/10.1016/S0304-8853(02)01279-9.

[65] H. Salazar-Tamayo, K.E. Garcia, C.A. Barrero, New method to calculate Mössbauer recoilless f-factors in $NiFe_2O_4$. Magnetic, morphological and structural properties, J. Magn. Magn. Mater. 471 (2019) 242–249, https://doi.org/10.1016/j.jmmm.2018.09.066.

[66] M.A. Gabal, Y.M. Al Angari, M.W. Kadi, Structural and magnetic properties of nanocrystalline $Ni_{1-x}Cu_xFe_2O_4$ prepared through oxalates precursors, Polyhedron 30 (2011) 1185–1190, https://doi.org/10.1016/j.poly.2011.01.032.

[67] D.M. Jnaneshwara, D.N. Avadhani, B.D. Prasad, H. Nagabhushana, B. M. Nagabhushana, S.C. Sharma, S.C. Prashantha, C. Shivakumara, Role of Cu^{2+} ions substitution in magnetic and conductivity behavior of nano-$CoFe_2O_4$, Spectrochim. Acta A Mol. Biomol. Spectrosc. 132 (2014) 256–262, https://doi.org/10.1016/j.saa.2014.04.179.

[68] Q. Li, C.W. Kartikowati, S. Horie, T. Ogi, T. Iwaki, K. Okuyama, Correlation between particle size/domain structure and magnetic properties of highly crystalline Fe_3O_4 nanoparticles, Sci. Rep. 7 (2017) 9894, https://doi.org/10.1038/s41598-017-09897-5.

[69] M. Maicas, M. Sanz, H. Cui, C. Aroca, P. Sanchez, Magnetic properties and morphology of Ni nanoparticles synthesized in gas phase, J. Magn. Magn. Mater. 322 (2010) 3485–3489, https://doi.org/10.1016/j.jmmm.2010.06.050.

[70] B. Dey, M. Bououdina, G.Abd elfadeel, P. Dhamodharan, S. AsathBahadur, M. Venkateshwarlu, C. Manoharan, Tuning the gas sensing properties of spinel ferrite $NiFe_2O_4$ nanoparticles by Cu doping, J. Alloy. Compd. 970 (2024) 172711, https://doi.org/10.1016/j.jallcom.2023.172711.

[71] M. Sukumar, J.R. Rajabathar, H. Al-Lohedan, S. Suresh, C.S. Dash, M. Sundararajan, P.S. Subudhi, S. Arokiyaraj, E. Yanmaz, S. Yuvaraj, R.S.R. Isaac, Synthesize and characterization of copper doped nickel ferrite nanoparticles effect on magnetic properties and visible light catalysis for rhodamine dye degradation mechanism, J. Alloy. Compd. 953 (2023) 169902, https://doi.org/10.1016/j.jallcom.2023.169902.